

# Complex Wavelet-Based Sinogram Segmentation for Metal Artifact Reduction in Cone-Beam CT

Siiri Rautio<sup>1</sup>, Alexander Meaney<sup>1</sup>, Salla-Maaria Latva-Äijö<sup>1</sup>, Harshit Agrawal<sup>2,3</sup>, Mikael Brix<sup>4,5</sup>, Dinidu Jayakody<sup>4</sup>, and Samuli Siltanen<sup>1</sup>

<sup>1</sup>Department of Mathematics and Statistics, University of Helsinki, Finland

<sup>2</sup>Department of Electrical Engineering and Automation, Aalto University School of Electrical Engineering, Finland

<sup>3</sup>Planmeca Oy, Finland

<sup>4</sup>Research Unit of Health Sciences and Technology, University of Oulu, Finland

<sup>5</sup>Department of Diagnostic Radiology, Oulu University Hospital, Finland

## Abstract

Metal objects pose a significant challenge in cone-beam computed tomography, as their strong and energy-dependent X-ray attenuation leads to inconsistent projections and severe streaking and shading artifacts in reconstructed images. These artifacts degrade image quality and limit the reliability of subsequent medical analysis. We propose a projection-domain metal artifact reduction method based on analytical metal segmentation in the three-dimensional sinogram using the three-dimensional Dual-Tree Complex Wavelet Transform, where directional wavelet coefficients are exploited to extract the wavefront set and singular support of metal structures. The resulting segmentation enables projection-domain inpainting and artifact-reduced reconstruction by combining metal-free and metal-only reconstructions. The proposed approach is evaluated on both simulated and clinical cone-beam computed tomography data and consistently reduces metal artifacts compared to conventional image-domain hard-thresholding methods. The results demonstrate improved visual quality and robustness in clinically realistic scenarios, highlighting the potential of analytically grounded, non-learned projection-domain segmentation for metal artifact reduction.

## 1 Introduction

In medical computed tomography (CT) imaging, metals appear in, for example, dental implants and orthodontic braces. Compared to biological tissues, metallic materials attenuate and scatter X-rays more strongly and highly non-uniformly across the X-ray energy spectrum, leading to inconsistent X-ray projections. These inconsistencies introduce severe streaking and shading artifacts in reconstructed CT images [16, 11, 19], significantly degrading image quality and compromising downstream medical image analysis. Metal artifacts are often even more severe in cone-beam computed tomography (CBCT) due to greater scatter, lower tube voltage, and cone-beam effects [43].

Metal artifact reduction (MAR) aims to mitigate these detrimental effects. From a reconstruction viewpoint, MAR algorithms can be grouped into three main categories: model-based iterative reconstruction (MBIR-MAR), image-domain MAR (ID-MAR), and projection-domain MAR (PD-MAR). Notably, most MAR methods in the literature address the 2D CT setting rather than 3D CBCT [11, 43].

MBIR-MAR methods combine a physics-based observation model with image priors in an iteratively solved optimization problem. They can produce excellent results and provide a principled way to incorporate prior information, e.g., sparsity-driven approaches [15], total variation with inequality constraints [42], and polychromatic statistical reconstruction [10]. However, MBIR approaches are typically computationally expensive due to repeated reconstruction and forward projection, limiting its practical impact.

ID-MAR methods apply post-processing to reduce streaks in reconstructed images [32, 49, 31, 25]. Because they operate after reconstruction, lost or distorted structures may be difficult to recover with high fidelity.

PD-MAR methods act on the projection data before reconstruction by identifying metal-corrupted regions and completing the corresponding projections. Many PD-MAR approaches treat the corrupted measurements as missing data and perform data completion using neighboring information. Although interpolation-based methods are computationally efficient, interpolation errors in the sinogram can lead to secondary artifacts in the corrected reconstructions [11, 35]. Normalized MAR methods mitigate this issue by interpolating normalized projections using a prior image [35, 34]. After projection completion, a metal-only reconstruction can be inserted into the artifact-reduced one to obtain the final result.

PD-MAR is often viewed as consisting of two steps: (1) metal segmentation and (2) inpainting. Accurate segmentation is critical, and simple thresholding is often insufficient [11]. After segmentation, inpainting can be performed using either traditional algorithms or learning-based approaches.

Metal segmentation can be performed in either the image or sinogram domain. Image-domain segmentation is more intuitive and commonly used in practice. The most straightforward approach is thresholding to isolate high-attenuation regions, for example using adaptive thresholding [36, 9, 41]. While fast and simple, thresholding is sensitive to beam hardening and artifacts and may fail with overlapping tissues or metals of varying densities. In CBCT, where Hounsfield Unit (HU) values are less reliable than in CT, thresholding can also yield inaccurate metal boundaries. Nevertheless, a common workflow is to threshold in the image domain and forward project the resulting metal mask to obtain a metal trace in the sinogram. For example, [30] uses image-domain thresholding in dental CT before applying a fully connected network to refine a linearly interpolated sinogram. Atlas-based segmentation [40] can leverage anatomical priors, but requires accurate registration and may be brittle in complex cases.

Most PD-MAR methods therefore segment metal in the image domain and forward project the mask to the sinogram. Direct segmentation in the projection domain is comparatively less explored and also challenging: simple thresholding can be ambiguous due to overlaps and path-dependent attenuation, producing non-uniform and view-dependent metal traces. Nevertheless, addressing metal segmentation (and inpainting) directly in the projection domain is appealing, since it avoids introducing artifacts during reconstruction and allows the sinogram geometry to be exploited analytically.

Deep learning-based PD-MAR methods have become popular, see, e.g., [18, 20, 30, 3]. In many settings, learning-based MAR improves quantitative performance relative to classical approaches, although methods operating solely via sinogram enhancement tend to underperform image-domain approaches [19]. As an example, [18] proposes a conditional GAN for security CT, where metal is segmented by image-domain thresholding followed by morphological operations, then forward projected to generate a sinogram mask; the contaminated projections are removed from the original sinogram.

Machine learning-based segmentation methods, such as CNNs or U-Nets trained on real [22] or synthetic [5] CBCT data, can generalize across noise levels and artifact patterns. However, they require annotated training data and careful model development, and may be less transparent than analytical approaches. Moreover, in clinical environments, reliance on machine learning can increase regulatory complexity and approval timelines, since AI solutions are often classified as high-risk medical devices and are subject to evolving regulatory requirements across jurisdictions (e.g., MDR and the EU AI Act in Europe) [1]. Consequently, where feasible, conventional non-learned algorithms may be advantageous.

Despite the appeal of projection-domain MAR, most PD-MAR methods still rely on image-domain segmentation followed by forward projection to identify corrupted sinogram regions. This motivates analytical methods that perform robust segmentation directly in the projection domain.

To segment metals directly from the 3D sinogram, we propose a method based on the 3D Dual-Tree Complex Wavelet Transform (3D DT-CWT), which extends the DT-CWT to three dimensions [14, 47]. The 3D DT-CWT provides approximate shift invariance and directional selectivity, which are useful for analyzing 3D sinogram volumes. While the 2D DT-CWT has previously been used within iterative CT reconstruction for MAR [46], here we use the 3D DT-CWT to computationally extract the wavefront set corresponding to metal objects in the CBCT 3D sinogram volume, followed by morphological processing to obtain a segmentation. After segmentation, inpainting is performed in the projection domain to complete the MAR pipeline. We evaluate the method on clinical scanner data, including both clinical acquisitions and simulated metals.

The remainder of the paper is organized as follows. Section II reviews the framework of CBCT. Section III introduces the DT-CWT and describes its use for singularity extraction. Section IV presents the proposed MAR method step-by-step. Section V describes the comparison method based on image-

domain hard thresholding. Section VI describes the simulated and experimental datasets. Section VII details the quantitative evaluation metrics, and Section VIII presents the results. Finally, Section IX concludes with a discussion and directions for future work.

## 2 Cone-beam computed tomography

CBCT is a lightweight and low-cost alternative to conventional CT. In CBCT, the patient is scanned using a cone-shaped beam and an X-ray detector panel for direct 3D image reconstruction. The 2D projection images of the field of view (FOV) are acquired during a single rotation. CBCT scanning cuts the radiation exposure when compared to helical CT, as the scanning FOV is smaller and tightly cropped [24]. Common applications of CBCT are dental imaging [26], extremity imaging and orthopedic studies [37], and oral and maxillofacial imaging [6].

The benefits of CBCT are its mechanical simplicity, mobility, low cost, and high spatial resolution compared to conventional CT. However, the cone-shaped X-ray beam, slow rotation, and limited detector area may lead to artifacts and low temporal resolution. Furthermore, the increased scattering with CBCT produces inferior soft-tissue contrast, magnified metal artifacts, and poor HU stability, which have limited the widespread applicability of CBCT [26]. Metals are a significant source of artifacts in dental CBCT, which complicates clinical decision making [8]. To address these challenges, novel reconstruction algorithms and MAR algorithms tailored for CBCT are needed to increase diagnostic image quality [33, 48, 7, 38].

The projection data in CBCT imaging forms a 3D  $xyz$ -volume, also referred to as the 3D sinogram. Each  $xy$ -plane corresponds to a single 2D projection image, and the projection angle proceeds along the  $z$ -axis. Each  $xz$ -plane of the 3D projection data superficially resembles a conventional 2D sinogram. However, only data from the midplane, perpendicular to the axis of rotation and containing the X-ray point source, is a true sinogram in the sense of containing the Radon transform of the object in that plane [44].

CBCT geometry requires demanding reconstruction mathematics. The key problem with exact 3D reconstruction is that the three-dimensional sinogram does not represent a Radon space. There is a method to overcome this problem, but still, the assumption is that a complete set of Radon data is available [12]. For the popular circular X-ray trajectory used in most technical applications, a complete set of Radon data is not available. Luckily, there are approximation methods that can also deal with incomplete Radon data. The most frequently used method for cone-beam reconstruction is the Feldkamp-Davis-Kress (FDK) algorithm [17], which is an approximate extension of the 2D filtered backprojection (FBP) algorithm into 3D cone-beam geometry.

### 2.1 Metal artifacts in CBCT

Metals in the scanned object cause inconsistencies in the projection data, resulting in artifacts in the reconstruction. Metal artifacts typically appear as bright or dark streaks surrounding metal objects in the CBCT image, as dark regions between metal objects, and as cupping effects. The inconsistencies are due to a number of mechanisms, most importantly beam-hardening, scatter, noise, photon starvation, the non-linear partial volume effect, and aliasing [16, 11, 19]. The ramp filtering and backprojection in FDK reconstruction spread these inconsistencies into global artifacts. Compared to CT, metal artifacts are exacerbated in CBCT [43].

The standard reconstruction model in X-ray tomography is based on Beer-Lambert law, where the X-ray intensity registered at detector pixel  $p$  is

$$I(p) = I_0 e^{-\int_{\text{ray path}} \mu(x, y, z) ds}, \quad (1)$$

where  $I_0$  is the intensity of incident X-ray beam and  $\mu(x, y, z)$  is the distribution of attenuation coefficients in the object. However, clinical scanners use polychromatic X-ray sources, and the attenuation model must be extended to

$$I(p) = \int_0^{E_{\max}} I_0(E) e^{-\int_{\text{ray path}} \mu(x, y, z, E) ds} dE. \quad (2)$$

Metals attenuate different X-ray energies highly nonlinearly, and lower energy photons experience extremely strong attenuation, and the average beam energy increases, *i.e.* hardens, as it passes through the medium. Furthermore, due to beam-hardening, the ratio of photoelectric absorption and Compton scattering changes for the remaining higher energy photons, with Compton effects dominating. As a result, photon paths are altered and they are registered at the detector off the center line of the incident beam. These effects causes strong inconsistencies in the observed integral attenuation values. If photon starvation occurs, practically all photons along a given ray path are absorbed and very strong streak artifacts arise.

Metals can cause a very high portion of the incident radiation to be absorbed. Due to low photon counts, the signal registered behind metals is very noisy as result of photon Poisson statistics and detector electronic noise. The random noise effects are propagated across the image during reconstruction, resulting in streaking artifacts.

The finite detector pixel size and reconstruction grid size can lead to non-linear partial volume (NLPV) effects when a metal object only partially covers a given voxel, resulting in incorrect attenuation estimation. The finite number of projection directions can also lead to streak-like artifacts around metals due to aliasing.

### 3 3D dual-tree complex wavelet transform

Analogous to Fourier analysis, wavelet methods decompose a function into translated and scaled copies of a mother wavelet. Wavelets have proven highly effective in signal processing applications, such as image compression. However, standard discrete wavelet transforms (e.g. Haar or Daubechies) suffer from shift sensitivity and exhibit poor directional selectivity, particularly in higher dimensions. The dual-tree complex wavelet transform [27, 45] addresses these limitations by employing two parallel wavelet decompositions, which can be interpreted as the real and imaginary components of a complex-valued transform. This dual-tree construction yields approximate shift invariance and significantly improved directional selectivity, providing 28 distinct directions in three dimensions.

#### 3.1 Mathematical construction

The 3D DT-CWT consists of complex-valued scaling and wavelet functions. Consider a complex, approximately analytic wavelet  $\psi(x)$ , defined by

$$\psi(x) = \psi_h(x) + i\psi_g(x), \quad (3)$$

where  $\psi_h$  and  $\psi_g$  are the real and imaginary parts of  $\psi(x)$ , respectively, and associated with a high-pass filter  $H$ . Similarly, a complex scaling function  $\phi(x)$  is given by

$$\phi(x) = \phi_h(x) + i\phi_g(x), \quad (4)$$

and associated with a low-pass filter  $L$ . The real parts  $\psi_h$  and  $\phi_h$  correspond to the real components of the wavelet and scaling function, while  $\psi_g$  and  $\phi_g$  are the imaginary components. For computational purposes, we use finitely supported wavelets, yielding approximately analytic wavelets.

We define the complex wavelet coefficients  $d_\nu(j, n) \in \mathbb{C}$  by

$$\begin{aligned} d_\nu(j, n) &= \langle f, \Psi_{\nu, j, n} \rangle \\ &= \int_{\mathbb{R}^3} f(x, y, z) \Psi_{\nu, j, n}(x, y, z) dx dy dz, \end{aligned} \quad (5)$$

where  $j = 0, \dots, J$  represents the scale and  $n = (n_1, n_2, n_3) \in \mathbb{Z}^3$  denotes the spatial index. The index  $\nu$  represents the oriented subbands, and there are 28 distinct directional subbands at each scale  $j$ , indexed by:

$$\mathcal{I} = \{ \bar{L}HH, \bar{H}LH, \bar{H}HL, LHH, HLH, HHL, HHH, \bar{H}\bar{H}H, \bar{H}\bar{H}\bar{H}, \bar{L}HL, \bar{L}LH, \bar{H}HH, \dots \}.$$

These 28 subbands represent the high-pass (detail) information in the transform, oriented in different directions along the three spatial dimensions. The subbands correspond to combinations of separable

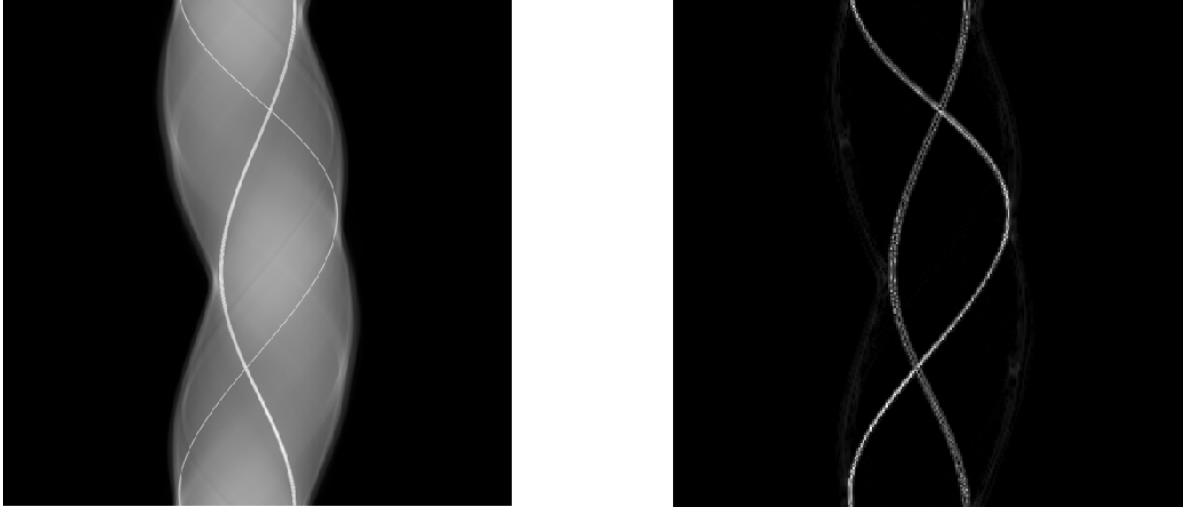


Figure 1: Sinogram (left) and the sum of the absolute value of the largest complex wavelet coefficients, revealing the location of the metals (right).

high-pass filters across the three axes, with each of the 7 fundamental orientations being replicated across 4 distinct quadrants (combinations of positive/negative real and imaginary parts).

The 3D wavelets are constructed as tensor products of the 1D scaling and wavelet functions. For example, the wavelet in the subband  $HHH$  is defined by:

$$\begin{aligned} & \Psi_{HHH,j,n}(x, y, z) \\ &= \psi(2^j x - n_1) \psi(2^j y - n_2) \psi(2^j z - n_3). \end{aligned} \quad (6)$$

Similarly, for a conjugate subband, such as  $\overline{HHH}$ , we have:

$$\begin{aligned} & \Psi_{\overline{HHH},j,n}(x, y, z) \\ &= \overline{\psi(2^j x - n_1)} \psi(2^j y - n_2) \psi(2^j z - n_3). \end{aligned} \quad (7)$$

In this manner, each of the 28 subbands corresponds to a distinct combination of wavelet functions along the three coordinate axes, yielding directional wavelets with high selectivity in 3D.

For discrete 3D images of size  $2^J \times 2^J \times 2^J$ , the indices  $n_1, n_2, n_3$  range from 0 to  $2^j - 1$  for each scale  $j$ . The transform starts at the finest scale, applying the analysis filters to the voxel data, and proceeds toward coarser scales by filtering the low-pass subbands.

The function  $f$  can be reconstructed from its coefficients via:

$$f(x, y, z) = \sum_{\nu \in \mathcal{I}} \sum_{j=1}^J \sum_{n_1=0}^{2^j-1} \sum_{n_2=0}^{2^j-1} \sum_{n_3=0}^{2^j-1} d_\nu(j, n) S^{-1} \Psi_{\nu,j,n}(x, y, z). \quad (8)$$

where  $S = T^*T$  is the frame operator, with  $T$  being the analysis operator and  $T^*$  the synthesis operator.

### 3.2 Wavelets in singularity extraction

The wavefront set  $WF(f)$  characterizes both the spatial locations and the orientations of singularities of a function. Let  $f \in L^2_{loc}(\mathbb{R}^2)$ . We say that  $f$  is microlocally smooth at  $x_0$  if one can find a cutoff function  $\phi \in C_c^\infty$  with  $\phi(x_0) \neq 0$  such that the Fourier transform of the localized function  $\phi f$  decreases faster than any polynomial in  $|\xi|$  as  $|\xi| \rightarrow \infty$ . If no such rapid decay occurs, then  $x_0$  lies in the singular support of  $f$ .

Directional information is obtained by examining the decay of the localized Fourier transform within angular regions of the frequency domain. If decay is not rapid inside a conical neighborhood

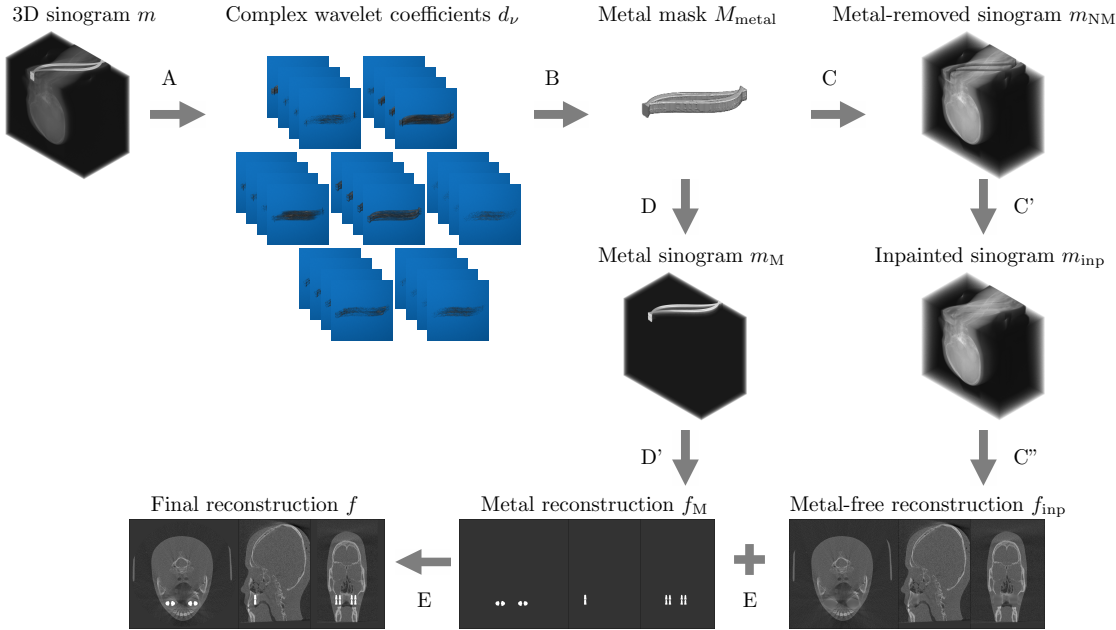


Figure 2: The proposed workflow for metal artifact reduction, based on projection-domain metal segmentation. Steps include: A. Extracting the wavefront set related to metals from the 3D sinogram. B. Binary mask for metal segmentation. C. Sinogram inpainting and metal-free reconstruction. D. Metal reconstruction. E. Final result: combining the artifact-free inpainted reconstruction and metal reconstruction.

centered at direction  $\theta_0$ , then  $(x_0, \theta_0)$  is an element of the wavefront set  $WF(f)$ . In imaging problems,  $\theta_0$  corresponds to the local edge orientation perpendicular to an interface.

In practice, the complex wavelet transform is an effective tool for extracting singularities from a signal, as previously demonstrated for CT wavefront set extraction in [39]. In images and volumetric data, large-magnitude wavelet coefficients typically occur near jumps and edges. See Fig. 1 for an example of a sinogram containing two metal inserts, where the sum of the absolute values of the wavelet coefficients reveals the corresponding metal boundaries.

The DT-CWT offers directional selectivity with moderate redundancy and computational efficiency. Real-valued wavelets provide only limited orientation discrimination, while curvelets [13] and shearlets [28, 29] achieve finer directional resolution at increased computational cost. For large 3D volumes, the DT-CWT provides a suitable balance between directionality and computational feasibility.

## 4 Proposed method

We propose a MAR method for projection-domain metal segmentation and inpainting, that uses 3D DT-CWT to find the edges of metals in the 3D sinogram. Fig. 2 shows the full workflow from 3D sinogram to metal artifact reduced reconstruction. The method is explained in detail below.

### 4.1 Extracting the wavefront set related to metals

We start with the 3D sinogram  $m \in \mathbb{R}^{x \times y \times z}$  as the input, and take the DT-CW transform of it, resulting in 28 detail coefficient subbands  $d_\nu(j, n) \in \mathbb{C}^{28 \times n}$ , where  $\nu = \{1, \dots, 28\}$  is the subband index and  $n = xyz$  is the number of voxels. Metals are highly attenuating, so they correspond to large wavelet coefficient values. We threshold away the smallest coefficients related to noise and non-metal features, by keeping only the largest coefficient values:

$$\tilde{d}_\nu(j, n) = (d_\nu(j, n) < \text{threshold}) \rightarrow 0.$$

Note that coefficient thresholding might not fully eliminate non-metal contributions, since superimposed structures in the 3D sinogram may also generate singularities detected by the DT-CWT,

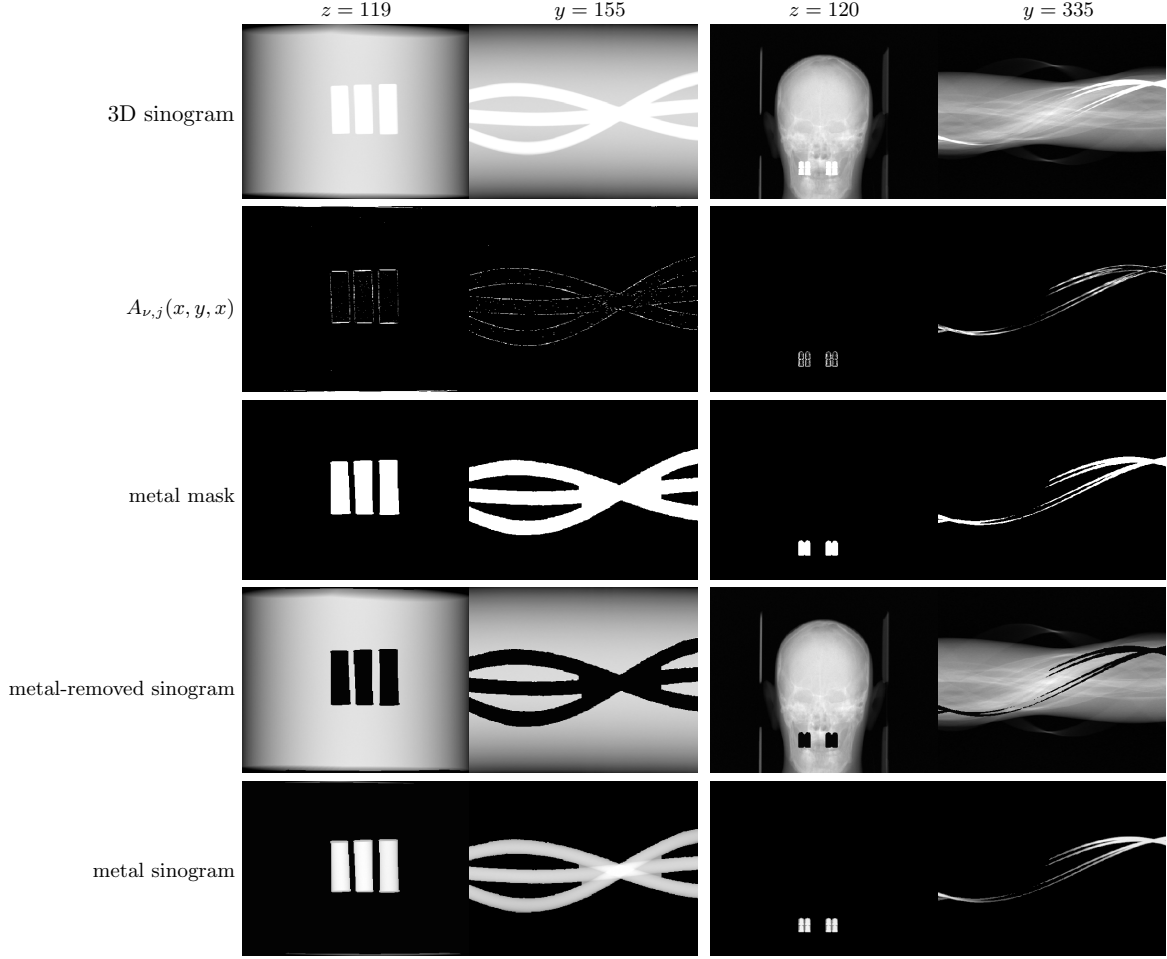


Figure 3: Metal segmentation results for simulated cases (I) and (II), presenting  $xy$ - and  $xz$ -slices of the 3D CBCT sinograms. Note that the metal mask slightly overshoots the metal area over the neighboring slice due to the morphological closing operation.

potentially leaving residual coefficients in the subbands  $\widetilde{d}_\nu(j, n)$ . This will be addressed in the next step.

## 4.2 Binary mask for metal segmentation

To move from the complex wavelet coefficient space  $\mathbb{C}^{28 \times x \times y \times z}$  to the 3D sinogram space  $\mathbb{R}^{x \times y \times z}$ , we take a sum over the absolute value of the thresholded coefficients:

$$A_{\nu,j}(x, y, z) = \sum_{\nu=1}^{28} |\widetilde{d}_\nu(j, n)|, \quad (9)$$

revealing the locations in the 3D sinogram space corresponding to the largest coefficients. See the 2nd row of Fig. 3 for an illustration of the resulting point cloud  $A_{\nu,j}(x, y, z)$  for two different 3D sinograms. Then, the result is binarized to  $B(x, y, z) \in \{0, 1\}^{x \times y \times z}$  by:

$$B(x, y, z) = \mathbf{1}(A_{\nu,j}(x, y, z) > 0), \quad (10)$$

where  $\mathbf{1}$  denotes the indicator function.

As mentioned in the previous subsection, the binary point cloud  $B(x, y, z)$  might still have voxels that are not related to a true metal trace, due to superimposition of features in the 3D sinogram. To remove these residuals, we leverage the geometric structure of sinograms and discard isolated voxels that do not align along a continuous geometric trajectory in the  $z$ -direction. That is, a voxel is retained

only if it has nonzero support within an  $n_h$ -neighbourhood in the  $(x, y)$  plane in at least  $d$  neighbouring slices along the  $z$ -direction, within a prescribed depth  $d$ :

$$\begin{aligned} & C(x, y, z) \\ &= B(x, y, z) \mathbf{1} \left( \exists t \in \{1, \dots, d\} \text{ such that} \right. \\ & \quad \left. \sum_{(x', y') \in \mathcal{N}_{n_h}(x, y)} B(x', y', z+t) + B(x', y', z-t) > 0 \right). \end{aligned} \quad (11)$$

with neighbourhood

$$\mathcal{N}_{n_h}(x, y) = \{(x', y') : |x' - x| \leq n_h, |y' - y| \leq n_h\}.$$

Voxels that fail this connectivity test are removed as isolated noise. By iterating this procedure, the remaining structures exhibit coherent propagation across slices, resembling the flow of information in a CBCT sinogram. The resulting values  $C(x, y, z) \in \{0, 1\}^{x \times y \times z}$  form a point cloud that corresponds to the singular support of the metal traces in the 3D sinogram space.

Next, we convert  $C(x, y, z)$ , which contains points located on metal boundaries, into a full binary mask for metal segmentation. Since the extracted boundary may not form a closed surface, we complete it using standard morphological operations [21]. In particular, we apply morphological closing, which consists of a dilation followed by an erosion using the same structuring element  $S \subset \mathbb{Z}^3$ .

The morphological closing of a set  $\mathcal{D}$  by a structuring element  $S$  is defined as

$$\mathcal{D} \bullet S = (\mathcal{D} \oplus S) \ominus S, \quad (12)$$

where  $\oplus$  and  $\ominus$  denote morphological dilation and erosion, respectively.

In our implementation, we apply morphological closing to  $C(x, y, z)$  using a spherical structuring element  $b$  of radius 3, yielding

$$\tilde{C}(x, y, z) = C(x, y, z) \bullet b_{r=3}. \quad (13)$$

After the boundary has been closed, the interior is filled using a flood-fill operation (MATLAB's 'imfill' function). The resulting binary mask  $M_{\text{metal}} \in \{0, 1\}^{x \times y \times z}$  represents the segmented metal regions in the 3D sinogram (see the third row of Fig. 3).

### 4.3 Sinogram inpainting and metal-free reconstruction

Using the metal mask  $M_{\text{metal}}$ , voxels corresponding to metal structures are segmented from the original 3D sinogram  $m$ , yielding a metal-removed sinogram  $m_{\text{NM}}$ . See the fourth row of Fig. 3. The missing regions are filled using harmonic inpainting by solving the discrete Laplace equation within the masked region subject to Dirichlet boundary conditions prescribed by the surrounding known pixel values using MATLAB's 'regionfill' function.

Each  $xy$ -projection of the 3D sinogram is inpainted independently. Inside the metal mask  $M_{\text{metal}}$ , the inpainted values are defined as the solution of the discrete harmonic equation

$$m_{\text{inp}}(x, y, z) = \frac{1}{4} \sum_{(i, j) \in \mathcal{N}(x, y)} m_{\text{inp}}(i, j, z), \quad (14)$$

where  $(x, y) \in M_{\text{metal}}(\cdot, \cdot, z)$ , and  $\mathcal{N}(x, y)$  denotes the four-connected neighborhood in the  $xy$ -plane. Values outside the mask are kept fixed to the original projection, imposing Dirichlet boundary conditions.

After the metals have been inpainted from the 3D sinogram, a reconstruction is computed using the FDK algorithm. The reconstruction  $f_{\text{inp}}$  does not include metals and, as such, should have reduced metal artifacts.

### 4.4 Metal reconstruction

For the final result, the metal components need to be added back into the inpainted reconstruction  $f_{\text{inp}}$ . To this end, the metals are reconstructed from a metal-only 3D sinogram obtained via metal segmentation, using the mask  $M_{\text{metal}}$ . The resulting metal FDK reconstruction  $f_M$  contains artifacts due to the inaccurate monochromatic approximation of the polychromatic Beer–Lambert law, as discussed in Section 2.1. However, since  $f_M$  consists solely of metal objects on an otherwise empty background, these artifacts can be readily removed by thresholding, thereby retaining only the metal information.

## 4.5 Final result

Finally, the metal reconstruction  $f_M$  is added to the metal-free reconstruction  $f_{\text{inp}}$ , yielding an artifact-free reconstruction with the metal objects restored.

## 5 Comparison methods

We benchmark the proposed method against metal segmentation based on hard thresholding (HT) in the image domain. This comparison method is referred to as HT-MAR throughout the paper. The threshold is selected in the range 2300–3000 HU, depending on the dataset. Following thresholding, the segmentation is morphologically opened using a spherical structuring element  $b_{r=3}$  to slightly expand the metal regions and better capture boundary voxels. The resulting segmentation is then forward-projected to obtain the corresponding metal mask in the projection domain for inpainting. All subsequent steps follow the same pipeline as in the proposed method.

Additionally, we evaluated hard thresholding directly in the projection domain. This approach proved ineffective and was therefore excluded from further analysis. The poor performance is due to the superposition of structures in the projections, which causes non-metal regions to exhibit high voxel values while, conversely, some metal features may not be distinctly visible. As a result, simple projection-domain thresholding fails to provide a reliable metal segmentation, as expected.

## 6 Datasets

We evaluate the proposed method using physical phantoms with both simulated and experimental metal inserts. The datasets with simulated metals include: (I) a PMMA phantom containing three simulated titanium inserts, and (II) an anthropomorphic phantom containing eight simulated amalgam inserts. In both cases, metal artifacts were simulated using a Monte Carlo-based X-ray transport simulator following [4, 2]. Specifically, we inserted metals in CT volumes and simulated primary and scattered projections along with flat-field projections for the geometry of Viso G7 CBCT device.

The experimental datasets include: (III) a tooth embedded in gelatin with an amalgam filling, (IV) a high-gold alloy fixed dental prosthesis, and (V) an anthropomorphic phantom containing a metal screw partially outside the reconstruction field of view.

All measurements were acquired using a Planmeca Viso G7 CBCT system. Measurements (I), (II), and (V) were performed at Planmeca Group, Helsinki, Finland, while measurements (III) and (IV) were obtained from [23], performed at the Medical Imaging Teaching and Test Laboratory (Mittlab), University of Oulu, Finland.

## 7 Quantitative Evaluation metrics

The precision of metal segmentation in the projection domain is evaluated in 3D using voxel-wise overlap between the predicted segmentation mask and the corresponding ground truth. We compute the Dice similarity coefficient,

$$D(A, B) = \frac{2 |A \cap B|}{|A| + |B|},$$

and the Jaccard similarity index,

$$J(A, B) = \frac{|A \cap B|}{|A \cup B|},$$

where  $A$  denotes the predicted segmentation and  $B$  the ground truth.

Segmentation metrics are computed only for datasets (I–II), for which ground-truth segmentations are available. For the comparison method (image-domain HT-MAR), the image-domain segmentation is forward-projected and subsequently binarized prior to metric evaluation.



Figure 4: Comparison of FDK reconstructions before correction and after artifact reduction using HT-MAR (comparison method) and CW-MAR (proposed method). Results are shown for physical phantoms with simulated metals (I-II) and experimental metals (III-V). For each phantom and method, axial, sagittal, and coronal slices are displayed. Reconstructions are not HU-calibrated. Visualization uses dataset-specific HU-equivalent windows to highlight metal-induced artifacts. Windowing (range, center): (I)  $[-1000, +1400]$  HU (200 HU), (II)  $[-2700, +5700]$  HU (1500 HU), (III)  $[-996, +186]$  HU ( $-405$  HU), (IV)  $[-998, -310]$  HU ( $-654$  HU), and (V)  $[-1240, -30]$  HU ( $-635$  HU).

Dataset	Metric	HT-MAR	CW-MAR
(I)	Dice	0.8375	<b>0.8876</b>
	Jaccard	0.7204	<b>0.7980</b>
(II)	Dice	0.8523	<b>0.8562</b>
	Jaccard	0.7426	<b>0.7486</b>

Table 1: Quantitative comparison of metal segmentation performance for the HT-MAR and proposed CW-MAR methods on datasets (I) and (II), using ground-truth masks derived from simulated metal inserts.

## 8 Results

We computed the uncorrected FDK reconstruction, the image-domain hard-thresholding-based MAR reconstruction, and the proposed projection-domain complex wavelet MAR reconstruction for datasets (I–V). Fig. 4 shows selected slices from the reconstruction volumes for each dataset, displayed using identical windowing. The quantitative results of the metal segmentation are reported in Table 1 for datasets (I) and (II).

Dataset (I) contains three simulated titanium inserts in an otherwise homogeneous PMMA phantom. Consequently, metal segmentation in both the image and projection domain is expected to be relatively straightforward. As seen in Fig. 4, the uncorrected FDK reconstruction exhibits substantial metal artifacts, which are particularly prominent in the axial slices. The HT-MAR method is able to reduce these artifacts to a large extent. However, residual artifacts remain near the metal boundaries as a result of imperfect segmentation. Even after morphological widening of the image-domain segmentation, the mask remains too narrow in some regions while being overly wide in others. This behavior is evidenced by the close-up reconstruction images and the segmentation metrics reported in Table 1. In contrast, the proposed CW-MAR method yields a more accurate projection-domain segmentation, resulting in an almost complete suppression of metal artifacts due to the tighter and more consistent segmentation.

Dataset (II) presents a considerably more challenging MAR problem, featuring eight metal implants in a more complex anthropomorphic phantom. The uncorrected FDK reconstruction is again heavily affected by metal artifacts, which are prevalent in all slicing directions and obscure many anatomical structures. The HT-MAR method is able to reduce these artifacts to a reasonable extent, with projection inpainting restoring much of the missing information. However, the estimated metal boundaries are somewhat inaccurate and include portions of bright artifact regions. The CW-MAR method captures the metal boundaries more robustly. Nevertheless, some room for improvement remains, as projection inpainting introduces mild blurring in the vicinity of the metal regions.

First of the experimental metal datasets, dataset (III) provides a simple test case for severe artifacts caused by an amalgam filling. As in dataset (I), the HT-MAR approach reduces artifacts in the uncorrected FDK reconstruction. However, residual artifacts persist due to missed metal voxels near the metal boundaries in the segmentation. The CW-MAR method removes nearly all artifacts, particularly in the sagittal and coronal slices.

Dataset (IV) produces substantial artifacts in the FDK reconstruction. For HT-MAR, identifying a suitable threshold level is challenging, as the HU values of the artifacts overlap with those of the actual metal features. This leads to poor metal segmentation. In contrast, CW-MAR removes most artifacts and recovers the general shape of the prosthesis.

Dataset (V) presents a particularly challenging MAR scenario, in which the metal object is partially outside the reconstruction field of view (FOV). As a result, streaking artifacts are present even when the metal itself does not appear within the reconstructed volume. The large screw produces severe artifacts in the uncorrected FDK reconstruction. The image-domain HT-MAR approach is unable to reduce artifacts caused by metals outside the reconstruction FOV and additionally struggles with accurate boundary segmentation, especially in the coronal direction, where the screw geometry is particularly challenging. In contrast, the CW-MAR method is not affected by metals outside the reconstruction FOV, since segmentation is performed in the 3D sinogram domain, where the corresponding metal trace is present. Consequently, artifact reduction is effective. However, as in previous cases, projection inpainting introduces some blurring, which in this dataset leads to a loss of fine anatomical detail.

## 9 Discussion and conclusion

This study investigated the use of the 3D dual-tree complex wavelet transform for metal segmentation in experimental 3D CBCT data. Segmentation was performed directly in the 3D sinogram domain and refined using morphological processing. The proposed method detected the wavefront set associated with metal inserts, enabling accurate projection-domain segmentation. After removing the metal traces and inpainting the resulting gaps, the reconstructed volumes exhibited substantially reduced metal artifacts. The metal components were subsequently reconstructed separately and reinserted without reintroducing metal-induced artifacts. These results indicate that the proposed 3D DT-CWT-based approach is a viable projection-domain method for metal artifact reduction in clinical 3D imaging, particularly in scenarios where metal objects lie partially outside the reconstruction field of view.

Future work will focus on improving performance in more challenging cases, especially by mitigating blurring in the vicinity of metallic objects. Potential directions include the use of more expressive multiscale representations, such as shearlets, and further refinement of the morphological processing of wavelet coefficients. While learned components may also be considered, purely analytical approaches retain practical advantages in clinical applications, where interpretability, robustness, and regulatory considerations are critical.

## Acknowledgment

This work was supported by Business Finland (decision no. 8132/31/2022), and by the Research Council of Finland through the Flagship of Advanced Mathematics for Sensing, Imaging and Modelling (grant no. 359182 and 359186) and the Centre of Excellence in Inverse Modelling and Imaging (grant no. 353097).

The authors would like to thank Annina Sipola and Ritva Näpänkangas from University of Oulu for arranging the prosthetic materials for datasets (III) and (IV).

## References

- [1] M. Aboy, T. Minssen, and E. Vayena. Navigating the EU AI act: implications for regulated digital medical products. *NPJ Digital Medicine*, 7(1):237, 2024.
- [2] H. Agrawal. *Deep learning-based metal and scatter artifact reduction in conebeam computed tomography*. PhD thesis, Aalto University, Espoo, Finland, 2025.
- [3] H. Agrawal, A. Hietanen, and S. Särkkä. Metal artifact reduction in cone-beam extremity images using gated convolutions. In *2021 IEEE 18th International Symposium on Biomedical Imaging (ISBI)*, pages 1087–1090. IEEE, 2021.
- [4] H. Agrawal, A. Hietanen, and S. Särkkä. Deep learning architecture for scatter estimation in cone-beam computed tomography head imaging with varying field-of-measurement settings. *Journal of Medical Imaging*, 11(5):053501–053501, 2024.
- [5] H. Agrawal, A. Hietanen, and S. Särkkä. Deep learning based projection domain metal segmentation for metal artifact reduction in cone beam computed tomography. *IEEE Access*, 11:100371–100382, 2023.
- [6] C. Angelopoulos, W. C. Scarfe, and A. G. Farman. A comparison of maxillofacial CBCT and medical CT. *Atlas of the oral and maxillofacial surgery clinics of North America*, 20(1):1–17, 2012.
- [7] M. Bal and L. Spies. Metal artifact reduction in CT using tissue-class modeling and adaptive prefILTERing. *Medical physics*, 33(8):2852–2859, 2006.
- [8] F. Bamberg, A. Dierks, K. Nikolaou, M. F. Reiser, C. R. Becker, and T. R. C. Johnson. Metal artifact reduction by dual energy computed tomography using monoenergetic extrapolation. *European radiology*, 21:1424–1429, 2011.

- [9] J. Bernsen. Dynamic thresholding of grey-level images. In *Proceedings of the 8th International Conference on Pattern Recognition*, 1986.
- [10] R. N. K. Bismark, R. Frysich, S. Abdurahman, O. Beuing, M. Blessing, and G. Rose. Reduction of beam hardening artifacts on real C-arm CT data using polychromatic statistical image reconstruction. *Zeitschrift für Medizinische Physik*, 30(1):40–50, 2020.
- [11] F. E. Boas and D. Fleischmann. CT artifacts: causes and reduction techniques. *Imaging Med*, 4(2):229–240, 2012.
- [12] T. M. Buzug. *Computed tomography: from photon statistics to modern cone-beam CT*. Springer, 2009.
- [13] E. J. Candès and D. L. Donoho. New tight frames of curvelets and optimal representations of objects with piecewise C2 singularities. *Communications on Pure and Applied Mathematics: A Journal Issued by the Courant Institute of Mathematical Sciences*, 57(2):219–266, 2004.
- [14] H. Chen and N. C. Kingsbury. Efficient registration of nonrigid 3-D bodies. *IEEE Transactions on Image Processing*, 21(1):262–272, 2012.
- [15] J. Choi, K. S. Kim, M. W. Kim, W. Seong, and J. C. Ye. Sparsity driven metal part reconstruction for artifact removal in dental CT. *Journal of X-ray Science and Technology*, 19(4):457–475, 2011.
- [16] B. De Man, J. Nuyts, P. Dupont, G. Marchal, and P. Suetens. Metal streak artifacts in X-ray computed tomography: A simulation study. *IEEE Transactions on Nuclear Science*, 46(3):691–696, 1999.
- [17] L. A. Feldkamp, L. C. Davis, and J. W. Kress. Practical cone-beam algorithm. *Journal of the Optical Society of America A*, 1(6):612–619, 1984.
- [18] M. U. Ghani and W. C. Karl. Fast enhanced CT metal artifact reduction using data domain deep learning. *IEEE Transactions on Computational Imaging*, 6:181–193, 2019.
- [19] L. Gjesteby and others. Metal artifact reduction in CT: where are we after four decades? *Ieee Access*, 4:5826–5849, 2016.
- [20] T. Gomi, R. Sakai, H. Hara, Y. Watanabe, and S. Mizukami. Development of a denoising convolutional neural network-based algorithm for metal artifact reduction in digital tomosynthesis for arthroplasty: A phantom study. *PLoS One*, 14(9):e0222406, 2019.
- [21] R. C. Gonzalez and R. E. Woods. *Digital image processing*. Pearson, 2018.
- [22] M. A. A. Hegazy, M. H. Cho, M. H. Cho, and S. Y. Lee. U-net based metal segmentation on projection domain for metal artifact reduction in dental CT. *Biomedical Engineering Letters*, 9:375–385, 2019.
- [23] D. Jayakody and others. A hybrid approach combining dual-energy and inpainting methods for metal artifact reduction in dentomaxillofacial CBCT: A proof-of-concept phantom study. *Annals of Biomedical Engineering*, 53(10):2638–2647, 2025.
- [24] W. A. Kalender. *Computed tomography: fundamentals, system technology, image quality, applications*. John Wiley & Sons, 2011.
- [25] G. Khaleghi, M. Hosntalab, M. Sadeghi, R. Reiazi, and S. R. Mahdavi. Metal artifact reduction in computed tomography images based on developed generative adversarial neural network. *Informatics in Medicine Unlocked*, 24:100573, 2021.
- [26] T. Kiljunen, T. Kaasalainen, A. Suomalainen, and M. Kortesniemi. Dental cone beam CT: A review. *Physica Medica*, 31(8):844–860, 2015.
- [27] N. C. Kingsbury. The dual-tree complex wavelet transform: a new efficient tool for image restoration and enhancement. In *9th European Signal Processing Conference (EUSIPCO 1998)*, pages 1–4. IEEE, 1998.

[28] G. Kutyniok and D. Labate. *Shearlets: Multiscale analysis for multivariate data*. Springer Science & Business Media, 2012.

[29] D. Labate, W. Q. Lim, G. Kutyniok, and G. Weiss. Sparse multidimensional representation using shearlets. In *Wavelets XI*, volume 5914, page 59140U. International Society for Optics and Photonics, 2005.

[30] D. Lee, C. Park, Y. Lim, and H. Cho. A metal artifact reduction method using a fully convolutional network in the sinogram and image domains for dental computed tomography. *Journal of digital imaging*, 33:538–546, 2020.

[31] K. Liang, L. Zhang, Ho. Yang, Y. Yang, Z. Chen, and Y. Xing. Metal artifact reduction for practical dental computed tomography by improving interpolation-based reconstruction with deep learning. *Medical Physics*, 46(12):e823–e834, 2019.

[32] H. Liao, W. A. Lin, S. K. Zhou, and J. Luo. ADN: artifact disentanglement network for unsupervised metal artifact reduction. *IEEE Transactions on Medical Imaging*, 39(3):634–643, 2019.

[33] A. H. Mahnken et al. A new algorithm for metal artifact reduction in computed tomography: in vitro and in vivo evaluation after total hip replacement. *Investigative radiology*, 38(12):769–775, 2003.

[34] E. Meyer, R. Raupach, M. Lell, B. Schmidt, and M. Kachelrieß. Frequency split metal artifact reduction (FSMAR) in computed tomography. *Medical physics*, 39(4):1904–1916, 2012.

[35] E. Meyer, R. Raupach, M. Lell, B. Schmidt, and M. Kachelrieß. Normalized metal artifact reduction (NMAR) in computed tomography. *Medical Physics*, 37(10):5482–5493, 2010.

[36] W. Niblack. An introduction to digital image processing. In *Prentice-Hall International*, 1986.

[37] PlanMed orthopedic imaging with Planmed Verity®. <https://www.planmed.com/computed-tomography/orthopedic-imaging/>. Accessed: 2025-05-08.

[38] D. Prell, Y. Kyriakou, M. Beister, and W. A. Kalender. A novel forward projection-based metal artifact reduction method for flat-detector computed tomography. *Physics in Medicine & Biology*, 54(21):6575, 2009.

[39] S. Rautio, R. Murthy, T.A. Bubba, M. Lassas, and S. Siltanen. Learning a microlocal prior for limited-angle tomography. *IMA Journal of Applied Mathematics*, 88(6):888–916, 2023.

[40] T. Rohlfsing, R. Brandt, R. Menzel, and C. R. Maurer. Evaluation of atlas selection strategies for atlas-based image segmentation with application to confocal microscopy images of bee brains. *NeuroImage*, 21(4):1428–1442, 2004.

[41] J. Sauvola and M. Pietikäinen. Adaptive document image binarization. *Pattern Recognition*, 33(2):225–236, 2000.

[42] C. Schiffer. TV-regularized CT reconstruction and metal artifact reduction using inequality constraints with preconditioning. *arXiv preprint arXiv:1810.03275*, 2018.

[43] R. Schulze and others. Artefacts in CBCT: a review. *Dentomaxillofacial Radiology*, 40(5):265–273, 2011.

[44] R. K. W. Schulze, D. Berndt, and B. d’Hoedt. On cone-beam computed tomography artifacts induced by titanium implants. *Clinical Oral Implants Research*, 21(1):100–107, 2010.

[45] I. W. Selesnick, R. G. Baraniuk, and N. C. Kingsbury. The dual-tree complex wavelet transform. *IEEE signal processing magazine*, 22(6):123–151, 2005.

[46] D. Us, U. Ruotsalainen, and S. Pursiainen. Combining dual-tree complex wavelets and multiresolution in iterative CT reconstruction with application to metal artifact reduction. *BioMedical Engineering OnLine*, 18(1):116, 2019.

- [47] B. Wang, Y. Wang, I. W. Selesnick, and A. Vetro. Video coding using 3D dual-tree wavelet transform. *EURASIP Journal on Image and Video Processing*, 2007(1):1–15, 2007.
- [48] J. Wei, L. Chen, G. A. Sandison, Y. Liang, and L. X. Xu. X-ray CT high-density artefact suppression in the presence of bones. *Physics in Medicine & Biology*, 49(24):5407, 2004.
- [49] Y. Zhang and H. Yu. Convolutional neural network based metal artifact reduction in x-ray computed tomography. *IEEE transactions on medical imaging*, 37(6):1370–1381, 2018.